FIVE-PHASE ELECTRIC MOTOR DESIGN FOR LIGHT SPORT AEROPLANE

D. Alban*, L. Brenner*, D. Gerling*
* University of the Bundeswehr Munich
Institute of Electric Drives and Actuators
Werner-Heisenberg-Weg 39, 85579 Neubiberg, Germany

Abstract

The project ELAPSED at the University of the Bundeswehr Munich investigates and develops electrical drivetrains and concepts for General Aviation. In this paper, the design of an electrical motor for Light Sport Aeroplanes (up to 600 kg takeoff weight) is discussed. Starting with the equations of motion and a propeller model, the requirements for the motor are derived from first principles. The typical design process of an e-motor is then described beginning with basic considerations about the size of the motor and key electromagnetic quantities. A stator with a concentrated winding and flux barriers, one of the main attributes of our design, is introduced. Finally, the motor is optimized to produce an efficient and light design for which the efficiency in the plane's operating points is calculated. This paper aims to provide a multi-disciplinary approach to aircraft e-motor design, illustrate the source of the motor requirements, as well as, the motor design so that aircraft engineers and e-motor designers can better cooperate.

Keywords
Airplane e-drive; Motor Design; Multi-phase; Stator Flux Barrier

1. INTRODUCTION

While electric mobility already plays a significant role in the automotive sector and will play a dominant role in the future, electric aviation is still in its early stages. The current field of application of electric drives in aviation is limited to small propeller-driven aircraft like LSA (Light Sport Aeroplane), as the technologies for storing electrical energy – batteries or hydrogen tanks combined with fuels cells – do not come close to the energy density of fossil sources.
In order for propeller-driven electric aircraft to be operated at all, the drive train and the electric machine in particular must be carefully designed and adapted to the application. Therefore, the first step requires a precise delineation of the application, i.e. the mission to be flown and the aircraft used. To be able to determine the characteristic values of the electrical machine from the flight values, an estimation between the power values of the propeller and those of the electric machine is required. One possible approach is to assume a constant propeller efficiency. By solving the steady-state equations of motion, it is already possible to quickly determine performance parameters for the drive, as shown in [1]. The use of a simple propeller model can further refine the design of the electric machine at an early stage of development.
The determination of the power parameters is followed by the design of the electric machine. For flight applications, this must be as light and efficient as possible, but at the same time very reliable. To meet these requirements, new designs with flux barriers in the stator and an increased number of phases are investigated. The design is carried out with increasing detail in order to control the complexity of the overall system. A pre-design is performed using analytical and empirical methods that provide an initial estimate of the parameters of the five-phase machine. From this initial design, optimization by means of finite element analysis (FEA) offers a way of maximizing the performance parameters of the machine within the same installation space.

2. E-PLANE REQUIREMENTS

To initially determine the performance parameters of a small electric aircraft, it is first necessary to specify the mission it must be able to fly. For this purpose, an exemplary flight profile is presented and a breakdown into the individual phases is made. From the description of the flight phases, the performance parameters of the propeller can be determined. These can be converted to the mechanical performance data of the electric machine by means of a propeller model.

2.1. General Aircraft Mission

The flight mission of an aircraft is characterized by different, clearly separated phases. In the simplest case, the flight phases are flown through in the sequence shown:

- Taxi
- Takeoff
- Climb
- Cruise
- Descent
- Landing

An example mission can be seen in Fig. 1 and shows the course of the altitude of the aircraft. The transitions between the listed flight phases are marked by the vertical dashed lines.
In an LSA, propulsive power is required from the propeller in all phases except descent and landing. For the determination of the required propulsion power, two-dimensional descriptions are often used for the calculation of the flight phases. The equations of motion are thus set up in x- and z-direction. Two basic conditions are distinguished for setting up the equations of motion. Either the aircraft has friction contact with the ground or it has no contact and is therefore in flight. For the case with contact to the ground,

doi: 10.25967/610390

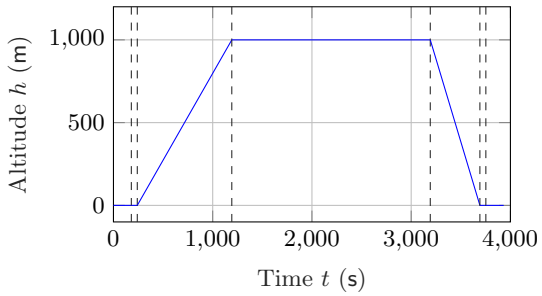

FIG 1. Exemplary mission profile.

the forces acting on the aircraft with their force application points are shown in Fig. 2. The thrust T, the aerodynamic forces lift L and drag D, the weight force W, as well as the contact forces N with the resulting rolling resistance forces μN, with μ as rolling resistance coefficient, provide for the movement of the airplane, which stands on a place with a slope φ. The equations of motion can be set up from the force equilibria in the drawn coordinate axes x and z, where x is defined in the direction of travel and thus parallel to the direction of air flow. The force equilibrium in the z-direction provides (1) and is equal to zero while the aircraft has not yet taken off. The force equilibrium in the x-direction provides the second equation of motion for the case with frictional ground contact as shown in (2).

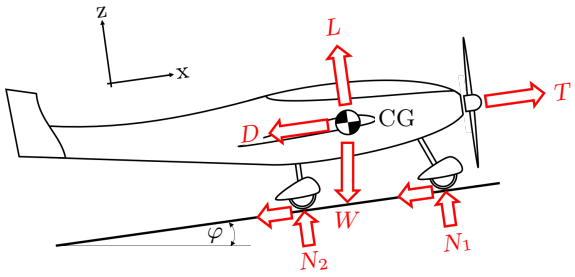

FIG 2. Free cut of the forces of an aircraft during takeoff, following [2].

$$\sum F_z = \frac{W}{g} a_z = W\cos\varphi - L - \underbrace{(N_1 + N_2)}_{N} \stackrel{!}{=} 0 \tag{1}$$

$$\sum F_x = \frac{W}{g} a_x = T - D - \mu N - W\sin\varphi \tag{2}$$

Fig. 3 shows the same aircraft in the air. Here, the contact forces and thus also the frictional forces are omitted. Instead, a new parameter, the angle of climb θ, is taken into account. The equations of motion for this case are shown in (3) and (4).

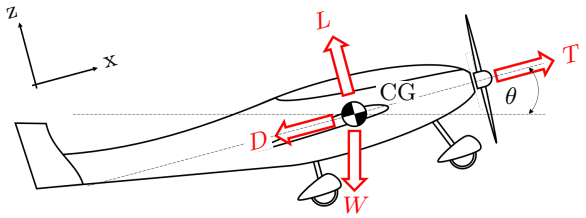

FIG 3. Free cut of the forces of an aircraft during climb, following [2].

$$\sum F_z = \frac{W}{g} a_z = L - W\cos\theta \tag{3}$$

$$\sum F_x = \frac{W}{g} a_x = T - D - W\sin\theta \tag{4}$$

To calculate a mission, assumptions are made about the mission and the aircraft that will fly it. The assumptions for the mission profile are listed in Tab. 1. The aircraft goes from taxi directly to takeoff, taking into account an acceleration time for the propeller. The takeoff and subsequent climb are flown at the constant maximum propeller speed and thus at maximum power. Shortly before reaching cruise altitude, the propeller speed is reduced to the rotational speed in cruise n_c and the cruise is completed at constant cruise altitude h_c. The subsequent descent and landing are assumed to be powerless. After landing a taxi segment completes the mission.

TAB 1. Mission Specifications

Parameter	Value	Unit
Runway distance s_{rw}	350	m
Cruise altitude h_c	2000	m
Cruise speed v_c	49	m/s
Time in cruise t_c	60	min
Taxi speed v_t	10	m/s
Time in taxi t_t	3	min

In addition to assumptions for the mission profile, assumptions are needed for the aircraft. A summary of the assumptions made is shown in Tab. 2. The value for the maximum takeoff mass $MTOM$ is taken from the european certification CS-LSA, while the other values are based on typical data for aircraft of this class. With the information on the required mission and the values for the aircraft weight and aerodynamic characteristics of the aircraft, performance values for the propeller can already be determined. However, for the determination of the power values of the electric machine from these values, a propeller model is needed which goes beyond the assumption of constant values for efficiency η_{prop} and thrust T.

TAB 2. Aircraft Specifications

Parameter	Value	Unit
Maximum takeoff mass $MTOM$	600	kg
Lift-to-drag ratio L/D	12	-
Propeller speed in cruise n_c	2300	rpm
Maximum propeller speed n_{max}	2500	rpm
Propeller diameter d_{prop}	1.6	m

2.2. Propeller Model

The propeller model presented here describes a fixed pitch propeller, i.e. a propeller where the pitch angle is fixed and cannot be changed in flight. With this type of propeller, thrust and efficiency are uniquely coupled via the advance ratio J.

$$J = \frac{v}{n \cdot d_{prop}} \tag{5}$$

The estimation of propeller thrust and efficiency is done with quadratic polynomials as a function of J. To set up these polynomials, characteristic values of the respective function are required. For the efficiency polynomial it is known that η_{prop} at $J = 0$ must also be $\eta_{\text{prop}} = 0$. As a second point, the location of the maximum efficiency is chosen with an estimated efficiency maximum of $\eta_{\text{prop,max}} = 0.8$. Since this value represents a maximum, the derivative of the polynomial at this point with $\partial\eta_{\text{prop}}/\partial J = 0$ is also known. The advance ratio at which $\eta_{\text{prop,max}}$ is reached is named J_η. The linear system for determining the efficiency polynomial can be seen in (6).

$$\begin{pmatrix} 0 & 0 & 1 \\ J_\eta^2 & J_\eta & 1 \\ 2 \cdot J_\eta & 1 & 0 \end{pmatrix} \begin{pmatrix} a \\ b \\ c \end{pmatrix} = \begin{pmatrix} 0 \\ \eta_{\text{prop,max}} \\ 0 \end{pmatrix} \tag{6}$$

The thrust requirement in cruise T_c can be determined directly from the resistance in cruise using (4). For the initial thrust, however, an iterative procedure is required. For this, the takeoff from standstill is calculated and the distance until lift-off is compared with the desired maximum takeoff distance s_{rw}. Then T_0 is adjusted and the calculation is carried out again until the error is smaller than a predefined threshold. The resulting linear system is shown in (7).

$$\begin{pmatrix} 0 & 0 & 1 \\ J_\text{c}^2 & J_\text{c} & 1 \\ 2 \cdot J_\text{c} & 1 & 0 \end{pmatrix} \begin{pmatrix} a \\ b \\ c \end{pmatrix} = \begin{pmatrix} T_0 \\ T_\text{c} \\ -T_\text{c}/J_\text{c} \end{pmatrix} \tag{7}$$

The polynomials for thrust and efficiency are calculated with the linear systems of equations (6) and (7). Their resulting curves are shown in Fig. 4 over the advance ratio J.

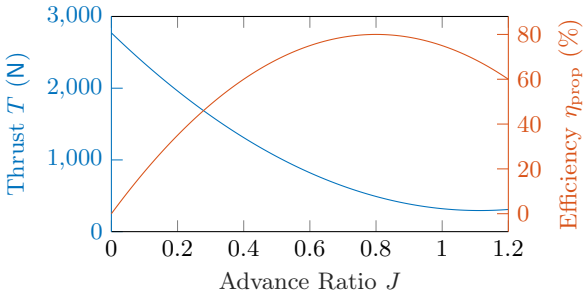

FIG 4. Resulting curves for thrust and efficiency of the modelled propeller.

It can be seen that the thrust of the propeller decreases with increasing degree of progress from its initial value T_0. In contrast, the efficiency of the propeller increases with increasing J up to the maximum value $\eta_{\text{prop,max}}$ which is just before advance ratio in cruise. After this maximum, η_{prop} decreases again. Since a quadratic function was chosen to model the propeller thrust, the thrust could increase with advance ratios $J > 1$. In order to preserve the informative value of the model, advance ratios higher than 1 should be avoided.

2.3. Power Requirement

With the equations of motion from 2.1 and the propeller model from 2.2, the desired mission can be calculated including the mechanical power of the propeller P_{prop} (continuous line) and the electric machine P_{em} (dashed line) in Fig. 5.

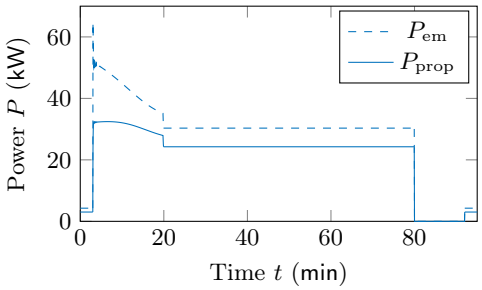

FIG 5. Resulting power for the electric machine P_{em} and the propeller P_{prop} for the mission under consideration.

The mission starts with constant power demand for electric machine and propeller in taxi. Once takeoff begins, the power and speed demands peaks for both systems. During climb the power demand on the propeller is decreasing, but with a lower rate than the power demand on the electric machine, since the efficiency of the propeller is increasing with its advance ratio J. After reaching cruise altitude h_c, power and speed demands on electric machine and propeller drop to constant values in cruise. Descent and landing are performed powerless. After reaching taxi speed in landing, power demand on electric machine and propeller are the same as in the first taxi phase, since the weight on a battery electric aircraft remains constant over the mission. The resulting profile for altitude and velocity for this mission can be seen in Fig. 6. It deviates from the mission profile shown in Fig. 1 since a constant rate of climb is not supported by the assumption that maximum available power is used for takeoff and climb. Oscillations occurring in the transition phases from takeoff to climb and from cruise to descent are a result of undamped rotational motion around the y-axis. The overall effect on the power demand on the electric machine is not significant, but in future versions of this tool a damping mechanism might be included.

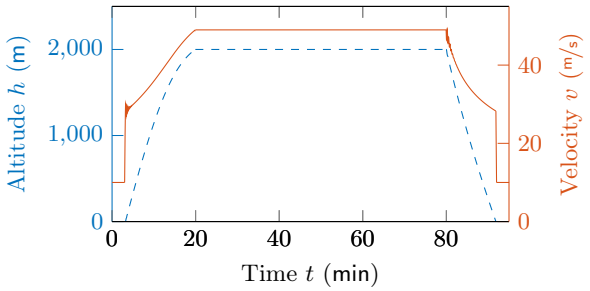

FIG 6. Resulting altitude and velocity profile for the mission under consideration.

The calculated power demands for the electric machine are summarized in Tab. 3. The highest power demand is found during takeoff, followed by the climb phase. Cruise is less power demanding, but still relevant in the design of the electric drive. Because of its comparatively long duration, it defines the needed continuous power of the components.

2.4. Design Objectives

Besides the performance requirements calculated from the mission and propeller model, the following points have been identified as key objectives for the design of an electric motor for airplanes:

TAB 3. E-Machine Power Demands

Parameter	Value	Unit
Maximum takeoff power $P_{\mathrm{to,max}}$	65	kW
Mean takeoff power $P_{\mathrm{to,mean}}$	51	kW
Propeller speed in takeoff n_{to}	2500	rpm
Maximum climb power $P_{\mathrm{climb,max}}$	53	kW
Mean climb power $P_{\mathrm{climb,mean}}$	43	kW
Propeller speed in climb n_{climb}	2500	rpm
Maximum cruise power $P_{\mathrm{c,max}}$	30	kW
Mean cruise power $P_{\mathrm{c,mean}}$	30	kW
Propeller speed in cruise n_{c}	2300	rpm

- Reliability: For obvious reasons, the reliability demands of an airplane propulsion drive are very high. Hence, a multi-phase approach has been chosen for the ELAPSED-prototype. Multi-phase motors have an increased fault tolerance in comparison to three-phase motors [3, 4]. The trade-offs are, among others, the increased complexity of the control of such motors and the higher number of power electronic switches which can drive the system's cost up. Weighing the advantages and the elevated system complexity, a five-phase motor has been favored for the ELAPSED prototype as the next feasible number of phases after three.
- Power density: Motor weight should be kept as low as possible while delivering the required power and torque.
- Efficiency: The motor should have a good efficiency in the operating points of the airplane. This keeps the losses lower and has a reinforcing effect on the size and weight of the battery system and inverter.

3. ELECTRIC MOTOR DESIGN

The electric motor design is performed based on the requirements and objectives derived in section 2. In general, the process of designing an electrical machine is a complex task that includes considerations of three main disciplines: electromagnetic, thermal and mechanical. The main focus of this paper is the electromagnetic design of an electric machine with regards to the power and speed demands of a pre-defined mission. The thermal and mechanical framework is set by using experience and literature values, as is common in an early stage of development of an electric machine.
The design process will be explained in this section: firstly, some pre-design decision are elaborated, followed by analytic calculations of the geometry. In the next chapter, the geometry is modeled in ANSYS Maxwell and the most influential parameters are then used in a multi-objective optimization to minimize the weight and the losses.

3.1. Motor Characteristics

Due to the large number of electrical machine types and design features, this section aims to justify the pre-selection decisions to reduce the number of free parameters for the design.

3.1.1. Motor Type: PMSM

The first step before the design is to select the motor type. There are many types of electrical machines based on their operation principle, each with their subcategories: DC machines, induction machines (IMs) (squirrel cage or slip rings), synchronous machines (SM) (electrically excited (EE), permanent magnets (PM)), reluctance machines (RM), among others.
A surface permanent magnet synchronous machine (SPMSM) is selected for the airplane application. This decision is justified by the superior power density of this machine type when equipped with powerful rare-earth magnets [5]. On the one hand, permanent magnets have a higher energy density than electromagnets, and on the other, they are free of Ohmic excitation losses. Thus, higher efficiencies and less overheating in the rotor are expected. Nevertheless, Eddy currents appear in the temperature sensitive magnets, especially as the frequency grows, that heat them and decrease their remanent flux density B_{r} and in the worst of cases completely demagnetize them. A further characteristic of PMSMs is the inability to vary the rotor excitation which is used in electrically excited synchronous machines (EESM) to control the voltage and imaginary power output. This is, however, not as significant for traction machines operating in isolation and no reason to favor an EESM over a PMSM for the airplane application where the power density is of utmost importance.
A design with surface permanent magnets is favored due to the higher air-gap flux density over one with interior PMs. IPMSMs are a popular choice in electric vehicles (EV) due to the large field-weakening constant power operation range, and the high mechanical forces that appear at high speeds which are better managed with an IPM design. In the airplane application, the maximum speed is around 2500 rpm (compared to over 10 000 rpm in EVs) and the centripetal forces on the magnets are thus not as critical. Additionally, since the propeller torque demand increases with speed, field-weakening cannot be exploited as in EVs where torque is reduced to reach higher speeds.

3.1.2. Fractional Slot Concentrated Winding

A fractional slot concentrated winding (FSCW) topology, see Fig. 7b, is selected for the ELAPSED motor. In comparison to the typical distributed windings, see Fig. 7a, FSCWs have are built with tooth-coils, and thus have shorter end windings that do not cross, lower Ohmic losses and a shorter axial construction space [6, 7]. Furthermore, the copper fill factor may be increased because of the simpler construction without coil end crossings. These two aspects should provide an advantage in the torque production over a comparable machine with a distributed winding. On the negative side, FSCWs produce a less sinusoidal magnetomotive force (MMF) and their air-gap field contains more harmonics which increase the losses in the iron lamination and the magnets.

3.1.3. Stator Flux Barriers

An additional motivation to select a FSCW is the possibility to combine it with stator flux barriers (FB) [8]. Flux barriers are placed in the stator to increase the torque of PM machines with FSCWs by influencing the air-gap flux density waveform, strengthening the working wave and weakening the main parasitic harmonic waves [9–11]. Further, the flux barriers can be used to cool the machine more effectively. Since the machine should be cooled with air to keep the system complexity low and avoid an additional point of failure with liquid cooling, air is directed through the FB to extract heat from the lamination stack.

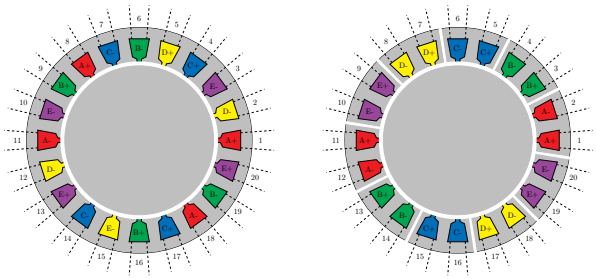

(a) Distributed winding, Q=20, p=3 (b) Concentrated winding with FB, Q=20, p=12

FIG 7. Distributed vs. Concentrated Winding (with FB)

3.2. Initial Parameters

In this section, the machine dimensions are calculated using simplified analytical expressions and empirical values for the main electromagnetic quantities.

3.2.1. Materials

The selection of the lamination and permanent magnets materials is often based on economical factors. Since the traction motor of an airplane will not account to a large portion of the airplane's total cost, and the quality and performance are critical, high-performance materials, listed in Tab. 4, can be selected.
A Cobalt-iron alloy with lamination thickness of 0.2 mm is selected for the stator and rotor. Cobalt-iron has a higher flux density saturation ($B_{\text{sat}} \approx 2.3\,\text{T}$) than the typical Silicon-iron alloys ($B_{\text{sat}} \approx 1.7\,\text{T}$). For highly utilized machines, this means that the machine can be constructed more compact. Neodymium-iron-boron (NdFeB) magnets have the highest energy density of all available permanent magnets. For the use in LSA and therefore in the aviation industry, which has a reduced cost pressure compared to other industries, the magnet strength N48 has been chosen, due to the availability of temperature resistant (up to 200 °C) and mechanically strong magnets. Finally, the coils will be made of enameled copper wire and the housing in Aluminium.

TAB 4. Motor Materials

Part	Material
Stator, Rotor	CoFe-alloy 0.2 mm
Permanent Magnets	NdFeB N48 200 °C
Coils	Enameled Copper Wire
Housing	Aluminium

3.2.2. Main Dimensions

The main dimensions of an electrical machine are its axial active length l_{Fe} and its air-gap diameter d_δ (or radius r_δ). They can be estimated by using empirical values for the peak air-gap flux density $\hat{B}_\delta \approx 1.1\,\text{T}$ (close to magnets B_r) and the rms current loading $A \approx 65\,000\,\text{A/m}$. The relationship between these two electromagnetic quantities and the tangential stress $\sigma_{\tan}$ is expressed by (8). With the rotor surface area $S_\text{r} = 2\pi r_\delta l_{\text{Fe}}$ and the lever radius r_δ the torque is obtained as a function of the tangential stress and the rotor volume, see (9). From these equations, and the calculated continuous torque in section 2, the rotor volume can be estimated. We use the continuous nominal torque, since the peak torque will only be needed for a reduced amount of time in which the machine will be driven in overload. With the length to radius ratio χ given in (11), it is possible to extract the length and the air-gap radius from the required volume [12].

$$\sigma_{\tan} = \frac{A\hat{B}_\delta}{\sqrt{2}} = \frac{65\,000\,\text{A/m} \cdot 1.1\,\text{T}}{\sqrt{2}} = 48\,260\,\text{Pa} \tag{8}$$

$$T = \sigma_{\tan} \cdot S_\text{r} \cdot r_\delta = 2\sigma_{\tan} \cdot \pi r_\delta^2 l_{\text{Fe}} \qquad T = 2 \cdot \sigma_{\tan} \cdot V_\delta \tag{9}$$

$$V_\delta = \frac{T_\text{N}}{2 \cdot \sigma_{\tan}} \qquad V_\delta = \frac{124.56\,\text{Nm}}{2 \cdot 48\,260\,\text{Pa}} = 0.001\,23\,\text{m}^3 \tag{10}$$

$$V_\delta = \pi r_\delta^2 l_{\text{Fe}} \quad \text{with} \quad \chi = \frac{l_{\text{Fe}}}{r_\delta} = \frac{\pi}{2p}\sqrt{p} \tag{11}$$

With the conditions elaborated in 3.1, the first six feasible five-phase FSCW topologies are summarized in Tab. 5, along with the estimated iron length and air-gap diameter. They all have the same rotor volume but their dimensions vary according to (11). Besides the 10- and 20-slot (Q) configurations, 30, and 40-slot topologies were part of the study, but are not shown in the table. From these configurations, however, the topologies with pole-pair number $p < Q/2$ can be discarded since the flux barriers would have to be located in the wounded teeth to strenghten the working harmonic . For $p > Q/2$, the flux barriers are placed in the unwounded teeth and the space between the FBs can be used to direct the air which is a critical feature of this motor design [13].

TAB 5. Initial Main Dimensions for six Configurations

Q	p	l_{Fe}	d_δ	FB
10	4	62.3 mm	158.7 mm	✗
10	6	54.4 mm	169.8 mm	✓
20	8	49.5 mm	178.1 mm	✗
20	9	47.5 mm	181.6 mm	✗
20	11	44.5 mm	187.8 mm	✓
20	12	43.2 mm	190.5 mm	✓

3.2.3. Stator Design

The remaining stator dimensions may be calculated now. Firstly, the tooth width can be estimated with (12) by using the ratio between the flux density in the air-gap to the one in the teeth $\gamma = \hat{B}_\delta/\hat{B}_\text{t} \approx 2$, since the saturation of the lamination material is around 2.3 T. The stacking factor k_{Fe} is set to 0.97.

$$w_\text{t} = \frac{l_{\text{Fe}} \cdot \tau_\text{s}}{k_{\text{Fe}} \cdot l_{\text{Fe}}} \cdot \gamma_\text{B} \tag{12}$$

The winding turns in series per phase N_s are selected so that the no-load induced voltage at the peak-power speed 2500 rpm is close under the maximum phase voltage in order to reach this point in the constant torque region. The phase voltage in the five-phase motor with a DC-link of $U_{\text{DC}} = 400\,\text{V}$ is $U_{\text{ph}} = 148.8\,\text{V}$ with space vector modulation which has a modulation factor $k_{\text{mod}} = 0.372$. With

the electrical angle frequency $\omega_{\mathrm{el}} = 2\pi \frac{n_{\max}}{60} \cdot p$, N_{s} is calculated with (13) where $\tau_{\mathrm{p}} = \frac{\pi d_\delta}{2p}$ is the pole-pitch and α_{p} the pole-pitch factor (in SPMSMs: the width of the magnet with respect to the pole-pitch). The pole-pitch factor is selected to reduce the parasitic harmonics in the rotor field with typical values between 0.83 and 0.87. Further, the fundamental winding factor k_{w1} is also included. The number of conductors z_{Q} in each slot, depending on the number of parallel coils per phase a is given by (14).

$$N_{\mathrm{s}} = \frac{\sqrt{2} \cdot U_{\mathrm{ph}}}{\omega_{\mathrm{el}} \cdot k_{\mathrm{w1}} \cdot l_{\mathrm{Fe}} \cdot \tau_{\mathrm{p}} \alpha_{\mathrm{p}} \cdot \hat{B}_\delta} \tag{13}$$

$$z_{\mathrm{Q}} = \frac{2 \cdot a \cdot m \cdot N_{\mathrm{s}}}{Q} \tag{14}$$

The required slot surface area is then obtained by first calculating the current from the power requirement with (15). The nominal power, as calculated in section 2, is $30\,\mathsf{kW}$, $m = 5$ phases and values for the efficiency $\eta = 0.93$ to 0.97 and the power factor $pf = 0.8$ to 0.9 must be initially chosen. Assuming a nominal conductor current density of $J_{\mathrm{N}} = 10\,\mathsf{A/mm^2}$ which is on the higher end of the obtainable density with air cooling, and a copper fill factor $k_{\mathrm{Cu}} = 0.40$ to 0.45, the slot area is given by (16). Now, the slot width is simply determined by subtracting the previously calculated tooth width from the slot pitch τ_{s} (17), while the slot height is derived from the area and width by assuming a rectangular slot form (18).

$$I_{\mathrm{ph}} = \frac{P_{\mathrm{N}}}{m \cdot \eta \cdot U_{\mathrm{ph}} \cdot pf} \tag{15}$$

$$S_{\mathrm{slot}} = \frac{z_{\mathrm{Q}} \cdot I_{\mathrm{ph}}}{a \cdot J_{\mathrm{N}} \cdot k_{\mathrm{Cu}}} \tag{16}$$

$$w_{\mathrm{s}} = \tau_{\mathrm{s}} - w_{\mathrm{t}} \quad \text{with} \quad \tau_{\mathrm{s}} = \frac{2\pi r_\delta}{Q} \tag{17}$$

$$h_{\mathrm{s}} = \frac{S_{\mathrm{slot}}}{w_{\mathrm{s}}} \tag{18}$$

Finally, the stator yoke height h_{ys} can also be determined by using guide values of flux density in this region $\hat{B}_{\mathrm{ys}} = 1.8\,\mathsf{T}$ to $2.0\,\mathsf{T}$ with (19), and the stator outer radius r_{so} is then obtained by adding the air-gap radius, slot height and yoke (20).

$$h_{\mathrm{ys}} = \frac{\alpha_{\mathrm{p}} \tau_{\mathrm{p}} \cdot \hat{B}_\delta \cdot l_{\mathrm{Fe}}}{2 \cdot k_{\mathrm{Fe}} \cdot l_{\mathrm{Fe}} \cdot \hat{B}_{\mathrm{ys}}} \tag{19}$$

$$r_{\mathrm{so}} = r_\delta + h_{\mathrm{s}} + h_{\mathrm{ys}} \tag{20}$$

3.2.4. Rotor Design

As discussed in 3.1.1, the rotor field is provided by surface permanent magnets (PM). In this type of machines, it is recommended to choose a short air-gap length δ to increase the torque. Considering manufacturing tolerances and allowing enough space for a retaining sleeve of $0.3\,\mathsf{mm}$, the air-gap length is fixed at $\delta = 0.8\,\mathsf{mm}$.
The PM height can be estimated with (21) assuming that the lamination permeability is infinite, so that the only magnetic voltage drops occur at the air-gap. This calculates the PM height based on the required current linkage at the magnet operating point where $B_{\mathrm{PM}} = \hat{B}_\delta$. However, it is also necessary to ensure that the magnets are not driven beyond their knee point and demagnetize by choosing the height to fulfill condition (22).

$$h_{\mathrm{PM}} = \delta \frac{\mu_{\mathrm{PM}}}{\mu_0} \cdot \frac{\hat{B}_\delta}{B_{\mathrm{r,PM}} - \hat{B}_\delta} \tag{21}$$

$$|H| > |\frac{\Theta}{h_{\mathrm{PM}}}| \tag{22}$$

3.2.5. Losses in E-Machines

There are two main loss components in electrical machines: copper and iron losses. The copper losses are conductive losses in the winding that are given by (23). The phase resistance R_{ph} is a function of the wire cross-sectional area and its length. Therefore, having short end windings reduces the resistance and losses. Frequency dependent losses that increase the resistance can also appear in the conductors due to the proximity and skin effects, but they are neglected here, since the wire diameter for the required voltage is smaller than the skin depth at the operating frequencies.
For the calculation of the iron losses, the Bertotti model computes the volumetric losses (24). It separates the iron losses in three components: hysteresis (factor k_{h}), eddy-current (k_{c}) and excess losses (k_{e}), each dependent on the electrical frequency and the flux density amplitude with a different power. The factors are computed from the loss information provided in electrical steel data sheets that provide losses at different frequencies and flux densities.

$$P_{\mathrm{Cu}} = m \cdot I_{\mathrm{ph}}^2 \cdot R_{\mathrm{ph}} \tag{23}$$

$$p_{\mathrm{Fe}} = k_{\mathrm{h}} f_{\mathrm{el}} \hat{B}^2 + k_{\mathrm{c}} \left(f_{\mathrm{el}} \hat{B}\right)^2 + k_{\mathrm{e}} \left(f_{\mathrm{el}} \hat{B}\right)^{1.5} \tag{24}$$

Additionally, conductive losses also appear in the magnets. Especially in SPMSMs, magnets must be segmented axially in order to contain the PM losses due to axial eddy currents.

4. FEA MODEL AND OPTIMIZATION

Finite Element Analysis (FEA) is the standard for the calculation and design of electrical machines. With it, magnetic and electric fields can be calculated and resulting forces evaluated. The dimensions obtained in section 3 are used to build the geometries in ANSYS Maxwell 2D with parameterized variables that permit to run an optimization. Since it is also desired to optimize the slot and pole number, for each candidate configuration (Q, p) a separate model is created. Depending on the symmetry of the topology, it is possible to split the model and use symmetry conditions to reduce the calculation time.

4.1. Model

Electrical machines have many parameters that can be varied which makes their design a challenging task. A general sketch of the geometry is depicted in Fig. 8 with the most relevant parameters, listed in Tab. 6, that have the highest impact on the machine's performance. To the parameters presented in section 3, two parameters for the flux barriers are added: the width of the flux barrier at the air-gap w_{FB}, and the angle α_{FB} that controls the inclination of the barrier. Furthermore, some parameters are expressed as ratios of others to guarantee feasible geometries. The split-ratio λ_{D} is used to get the air-gap radius from the stator outer radius and the PM width is controlled over the pole-pitch

factor α_p. In the models, the slots are designed such that the tooth walls are parallel on both sides to have homogeneous flux paths. The PMs have a bread loaf shape, i.e. they are flat on the rotor side for better adherence, and round on the air-gap end. The rotor yoke is intentionally omitted from the free parameters because material is anyway needed up to the shaft. In order to reduce the weight, cuts are made in the rotor lamination.

TAB 6. Free Parameters

Variable	Description
l_Fe	Axial active length
r_so	Stator Outer Diameter
$\lambda_\mathrm{D} = \frac{r_\delta}{r_\mathrm{so}}$	Split ratio
h_PM	Magnet height
$\alpha_\mathrm{p} = \frac{w_\mathrm{PM}}{\tau_\mathrm{p}}$	Pole-arc pitch
h_ys	Stator yoke height
w_t	Wounded tooth width
$w_\mathrm{t,FB}$	FB tooth width
w_FB	FB width
α_FB	FB angle

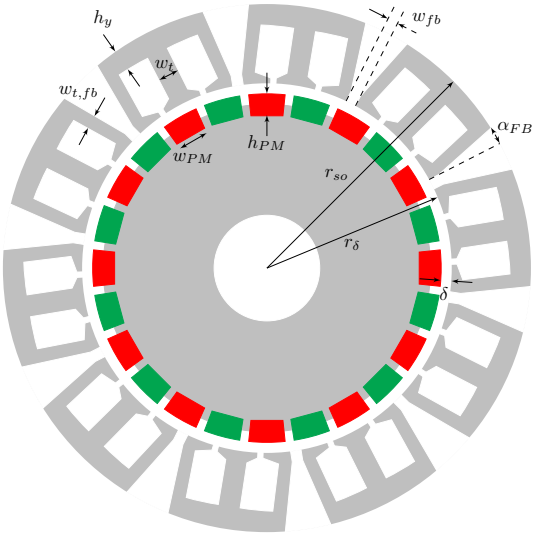

FIG 8. 2D Motor Model Sketch, Q=20, p=12.

The transient simulations are configured to calculate the fields over two electrical periods at a fixed speed and require under three minutes calculation time for each variation. The materials introduced in section 3.2.1 are assigned to the corresponding surfaces in the model. Furthermore, the magnetization direction of the magnets is defined by creating coordinate systems at each magnet in the radial direction. The excitation of the coils is defined with ideal sinusoidal signals with an amplitude computed from the assumed current density, the slot area and the copper fill factor, and a time shift of 72°.
Fig. 9 shows the flux density distribution of one of the models at a chosen time step. From the fields, other results are calculated such as the electromagnetic torque, the mechanical power, the induced voltage, the copper and iron losses, etc. The weight of the active parts can also be determined by multiplying the surface areas with the machine length and the corresponding material density. The rotor is accounted for as half the area (due to weight-saving holes) of a hollow cylinder with outer diameter at the PMs and inner diameter equal to the shaft's 45 mm. The mean end winding length for FSCWs is approximated with (25) and is also included in the weight calculation [14].

$$l_\mathrm{ew} \approx \frac{3\pi^2 \cdot (2 \cdot r_\delta + h_\mathrm{s})}{8 \cdot Q} \tag{25}$$

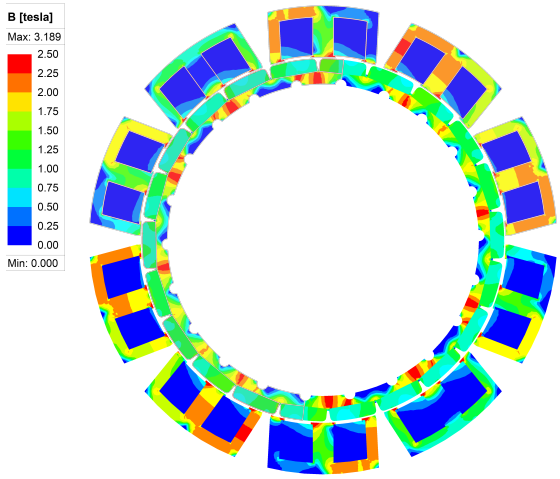

FIG 9. Flux Density Plot from FEA Model, Q=20, p=11.

4.2. Optimization

The geometry optimization is performed with ANSYS optiSLang which provides a user-friendly GUI for numerical optimizations that can be coupled to the Maxwell models. A direct multi-objective optimization is performed for each topology candidate with the objective function (26) that aims to minimize the weight (W) and the losses ($P_\mathrm{Cu} + P_\mathrm{Fe}$) at the peak operating point. The constraints are defined such that the resulting mechanical power is more than 65 kW, the torque ripple is less than 3.5 % and the power factor is larger than 0.8, see (27). The parameters of vector $\underline{x}$ are presented in Tab. 6 for which adequate ranges must be defined. The peak operating point is selected for the optimization because it is critical and must be achieved by the motor in the take-off phase. The peak current density is set to 20 A/mm^2, a high value that cannot be maintained continuously for thermal reasons. Nevertheless, an optimization with the same criteria but for the continuous operation point with $J_\mathrm{N} = 10\,\mathrm{A/mm^2}$ returns very similar geometries. Since the current density is fixed, the actual current is influenced only by the stator geometry, more exactly the slot area.

$$f_\mathrm{obj}(\underline{x}) = min(W, (P_\mathrm{Cu} + P_\mathrm{Fe})) \tag{26}$$

$$65\,\mathrm{kW} - P_\mathrm{mech} \leq 0$$

$$T_\mathrm{ripple} - 0.035 \leq 0 \tag{27}$$

$$0.8 - pf \leq 0$$

The selected optimization method is Adaptive Multi-Objective (AMO) which combines a Genetic Algorithm MO approach with Kriging to arrive at the global optimum with less samples. The optimizer calls an FEA simulation for each design variation and retrieves the relevant parameters and results. On a 16 core computer, the program is configured to call 15 parallel FEA simulations, and returns a solution within three hours for all

considered motor topologies. To evaluate the optimization results, a Pareto response graph, as the one in Fig. 10, is obtained for each candidate topology. The best results are highlighted with red and form the pareto front. The bold points represent feasible designs, while the empty squares correspond to design variations that did not meet all the constraints. Note that the two objectives cause opposite effects. The easiest method to improve the efficiency is constructing a bigger machine and lowering its utlization, i.e. lower current and flux density, which reduce the losses. Inversely, the weight is proportional to machine volume, which forces a high utilization of the motor.

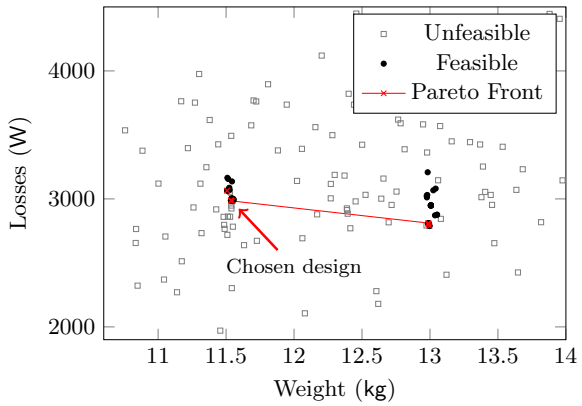

FIG 10. Pareto Front for Q=20, p=12

From eight studied topologies, the one with the best result was the one with 20 slots and 12 pole-pairs. Tab. 7 shows the weight and losses of a selection of optimized designs. As expected, the losses of the designs with higher pole-pair number are larger due to the frequency-dependent iron losses. These machines have a short axial length, a larger diameter and thinner yokes. If only the active material's weight was considered, they would be lighter. Nevertheless, as mentioned before, the rotor material has to be taken into account beyond the minimal required rotor yoke. Additionally the end windings, which scale with the air-gap radius, see (25) are also longer. For these two reasons, the weight advantage disappears and does not counterbalance the increase in losses. At the other extreme, the candidates with 10 slots do not use the stator space effectively, require very large slots and were also discarded due to their higher weight.

TAB 7. Optimization Results

Design	Weight (kg)	Losses (W)
$Q = 20$, $p = 11$	12.10	2923
$Q = 20$, $p = 12$	11.55	2986
$Q = 30$, $p = 18$	12.48	3848
$Q = 40$, $p = 22$	12.30	4152

4.3. Final Design

On the pareto plot of Fig. 10, the chosen design is marked by the arrow. This solution has slightly higher losses than the design with minimum losses but is about 1.5 kg lighter. The selected design undergoes final adjustments, its performance is verified and other performance values are evaluated. For example, one important indicator of the motor design is its the efficiency over the entire operation region. The efficiency map is generated using a surrogate model created from 100 FEA simlulations with varying current amplitude and angle and is depicted in Fig. 11. The efficiency values for the calculated flight phases are further summarized in Tab. 8. For this calculation, the magnet losses are neglected because their evaluation requires a 3D 'disc' FEA model with the axial length of one magnet segment. With an axial segmentation in 10 parts, the magnet losses amount to approximately 350 W for the peak operation and will be lower for all other points.

TAB 8. Final Design Efficiency

Op. Point	n_{Prop} (rpm)	T (Nm)	η (%)
Take-off max	2500	248	95.93
Take-off mean	2500	195	95.91
Climb max	2500	202	95.92
Climb mean	2500	164	95.82
Cruise	2300	125	95.52

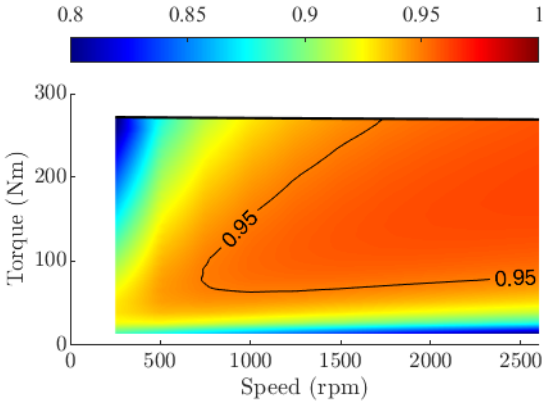

FIG 11. Efficiency Map

5. CONCLUSION

The performance requirements of the motor have been derived by considering an LSA mission. The power curve of a propeller airplane is roughly calculated to arrive at the mechanical requirements. The motor peak power results at 65 kW and a propeller speed of 2500 rpm. The continuous power in the cruise phase is 30 kW at 2300 rpm. With these operating points, the electromagnetic design of the machine is undertaken.

Besides the mechanical requirements, the weight, the reliability, and the efficiency are identified as key performance characteristics for an airplane motor. Based on these considerations, the pre-design decisions are explained before beginning the detailed motor development. In the first place, the motor is selected to be a permanent magnet synchronous machine (PMSM) due to the superior power density achievable with this motor type and the reduced rotor losses. Further, a fractional slot concentrated winding (FSCW) is favored over a distributed one. This winding has shorter overhangs which allow building machines with higher torque densities and lower copper losses. Furthermore, this winding can be combined with a flux barrier stator to increase the torque of the machine, decrease its weight, and improve its cooling behavior. For increased reliability, the motor phase number is selected to be five.

A preliminary design is performed with typical electric and magnetic values for adequate topology candidates (pole/slot combinations) and by selecting high-performance materials. These designs are modeled parametrically in ANSYS Maxwell 2D to perform transient electromagnetic Finite Element Analysis (FEA). Each topology is optimized for minimum weight and maximum efficiency. Since electrical machines have a large number of free parameters, only ten geometrical parameters are selected for the optimization. Finally, from the optimized designs, the best one is selected for further development. The final design, depicted in 3D in Fig. 12, will be manufactured, and the experimental validation of the prototype will be performed on a test bench and an "iron bird".

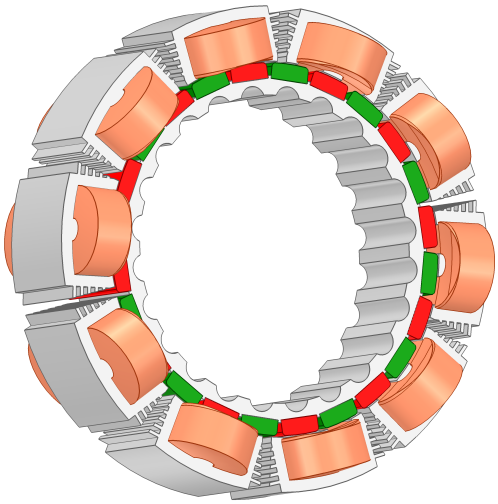

FIG 12. Final Design 3D Model

ACKNOWLEDGEMENTS

This research paper is funded by dtec.bw - Digitalization and Technology Research Center of the Bundeswehr. dtec.bw is funded by the European Union - NextGenerationEU

References

[1] S. Diecke. Electric aircraft performance analysis utilizing simplified approaches for airfoil and propulsion chain design. AIAA Aviation Forum, 2023. DOI: 10.2514/6.2023-3665.

[2] S. Gudmundsson. General Aviation Aircraft Design. Butterworth-Heinemann, Amsterdam, Netherlands, 1st ed. edition, 2014. ISBN: 978-0-12-397308-5. DOI: 10.1016/C2011-0-06824-2.

[3] I. Bolvashenkov, J. Kammermann, and H. G. Herzog. Research on reliability and fault tolerance of multiphase traction electric motors based on markov models for multi-state systems. In 2016 International Symposium on Power Electronics, Electrical Drives, Automation and Motion (SPEEDAM), pages 1166–1171, 2016. DOI: 10.1109/SPEEDAM.2016.7525928.

[4] E. Levi. Multiphase electric machines for variable-speed applications. IEEE Transactions on Industrial Electronics, 55(5):1893–1909, 2008. ISSN: 0278-0046. DOI: 10.1109/TIE.2008.918488.

[5] J. D. Widmer, R. Martin, and M. Kimiabeigi. Electric vehicle traction motors without rare earth magnets. Sustainable Materials and Technologies, 3:7–13, 2015. ISSN: 22149937. DOI: 10.1016/j.susmat.2015.02.001.

[6] J. Cros and P. Viarouge. Synthesis of high performance pm motors with concentrated windings. IEEE Transactions on Energy Conversion, 17(2):248–253, 2002. ISSN: 1558-0059. DOI: 10.1109/TEC.2002.1009476.

[7] F. Magnussen and C. Sadarangani. Winding factors and joule losses of permanent magnet machines with concentrated windings. In IEEE International Electric Machines and Drives Conference, 2003. IEMDC'03, pages 333–339 vol.1, 2003. DOI: 10.1109/IEMDC.2003.1211284.

[8] G. Dajaku and D. Gerling. A novel 12-teeth/10-poles pm machine with flux barriers in stator yoke. In 2012 XXth International Conference on Electrical Machines, pages 36–40, 2012. DOI: 10.1109/ICElMach.2012.6349835.

[9] J. W. Gerold and D. Gerling. Design rules for stators with flux barriers. In 2019 IEEE 13th International Conference on Power Electronics and Drive Systems (PEDS), pages 1–8, 2019. ISBN: 2164-5264. DOI: 10.1109/PEDS44367.2019.8998861.

[10] J. W. Gerold and D. Gerling. Analysis of different arrangements of flux barriers and different pole pairs in a stator with concentrated winding. In 2018 XIII International Conference on Electrical Machines (ICEM), pages 58–64. IEEE, 2018. ISBN: 978-1-5386-2477-7. DOI: 10.1109/ICELMACH.2018.8507208.

[11] D. Albán, G. Dajaku, and D. Gerling. Evaluation of flux-barrier stator in five-phase pmsms for electric aircraft traction. In 2022 25th International Conference on Electrical Machines and Systems (ICEMS), pages 1–6, 2022. ISBN: 2642-5513. DOI: 10.1109/ICEMS56177.2022.9983393.

[12] J. Pyrhönen, T. Jokinen, and V. Hrabovcová. Design of rotating electrical machines. Wiley, Chichester, England, 2nd ed. edition, 2014. ISBN: 9781118701591. DOI: 10.1002/9781118701591.

[13] J. W. Gerold and D. Gerling. An equivalent winding factor larger than 1 by using flux barriers in the stator. In 2019 IEEE International Electric Machines & Drives Conference (IEMDC), pages 1855–1862, 2019. DOI: 10.1109/IEMDC.2019.8785148.

[14] G. Huth. Permanent-magnet-excited ac servo motors in tooth-coil technology. IEEE Transactions on Energy Conversion, 20(2):300–307, 2005. ISSN: 1558-0059. DOI: 10.1109/TEC.2005.845537.